Geophysical Journal International

Geophys. J. Int. (2020) **223,** 632–647
Advance Access publication 2020 July 11
GJI Seismology

doi: 10.1093/gji/ggaa334

Effects of bathymetry complexity on tsunami propagation: a spherical harmonics approach

Amir Salaree[1,2] and Emile A. Okal[1]

[1]*Department of Earth and Planetary Sciences Northwestern University, 2145 Sheridan Rd, Evanston, IL 60208, USA. E-mail: salaree@umich.edu*
[2]*Department of Earth and Environmental Sciences University of Michigan, 1100 N University Ave, Ann Arbor, MI 48109, USA*

Accepted 2020 July 3. Received 2020 June 27; in original form 2020 February 29

SUMMARY

This paper explores the effects on tsunami simulations of the level of detail of the bathymetric grid in use. For this purpose, we expand available bathymetric data sets of the Pacific Basin in spherical harmonics. For realistic scenarios of tsunamis generated by earthquake dislocations, we conclude that an expansion to a maximum degree $l_{\max} = 40$, corresponding to wavelengths of 1000 km, is sufficient to reproduce the main features of the tsunami wavefield synthesized in deep water, that is, without considering final shoaling and interaction with coastal features.

Key words: Tsunami; Pacific Ocean; Numerical modelling; Earthquake hazards.

1 INTRODUCTION

The purpose of this paper is to explore the minimum level of bathymetric detail necessary to build acceptable transoceanic tsunami simulations for realistic models of earthquake sources. Bathymetric data quantify the depth of the ocean floor at various geographic points. The data are collected using various methods from ship soundings to satellite altimetry (e.g. Smith 1993; Smith & Sandwell 1994, 1997; Stumpf *et al.* 2003).

Bathymetry data sets are created by sampling the real ocean floor at various spatial resolutions. Therefore, they constitute models that are not exact representations of the real world, but simply approximate it. Higher sampling rates in bathymetry acquisition result in denser grids (Becker *et al.* 2009; Tozer *et al.* 2019) which, however, pose practical issues such as data storage limits and more importantly processing time (PMEL 2006), even though the latter may be expected to further decrease in the forthcoming years.

The issue of processing time also poses serious challenges in tsunami early warning and hazard mitigation (e.g. Reymond *et al.* 2012; AMS 2015). It is therefore of interest to find an optimal state where the bathymetric data resolution is high enough to represent the most crucial physical features, but is not too dense to obstruct efficient computing.

While working with bathymetric grids in tsunami simulations, it is important to differentiate between the physical (Res_p) and spatial (Res_s) resolutions. Spatial resolution of a bathymetry grid is simply a measure of the spacing of individual neighboring grid points. In other words, it corresponds to how densely a given set of bathymetric or topographic features are sampled. Physical resolution, however, is a measure of the amount of fine bathymetric details (slopes, seamounts, etc.) represented in the bathymetric data set used to create the grid.

Based on numerical experiments, Titov & Synolakis (1997) argued that Res_p has more effect on simulation results than Res_s, which they justified by noting that 'denser grids have identical physical resolutions as the coarse grids that produced them'. It is therefore critical to find the level of physical resolution adequate to correctly predict the main features in the propagation of a given tsunami.

1.1 Resolving detailed bathymetry

Numerous methods exist to reduce the level of spatial complexity in a given data set, a most common one being moving average filters (Smith 1999), which are routinely used to reduce physical details in bathymetric grids. Application of these filters is justified by the fact that they preserve the volume of the bathymetric features (Salaree 2019). In tsunami simulations, an empirical smoothness measure is chosen by each experimenter while working with bathymetric grids, depending on propagation features deemed important. Thus, it is of interest to determine a measurable, general framework for a potential level of bathymetric smoothness in tsunami simulations which can be adapted for any given case. While the smoothness level clearly depends on the problem at hand, it is very useful to obtain a robust metric that can be used to define such a threshold. However, the application of moving average filters to grids is challenged by the following factors:

(i) **Quantification:** Performance of moving average filters is difficult to quantify. While it is possible to interpret the geographic window size of these filters as a cut-off wavelength, one can show that smoothing of sparser (and not decimated) grids would lead to different results (Salaree 2019). These filters may be quantified through the percentage of points in the moving window relative to the total number of grid points, but this does not describe the final product because it depends significantly on the spatial resolution of the grid. As a result, one cannot uniquely express the performance of these filters in a quantitative scale.

(ii) **Altering the bathymetric slopes:** While moving average filters do preserve the volume of bathymetric features, they significantly alter the existing bathymetric slopes (e.g. Salaree 2019). Expansion filters such as spherical harmonics, on the other hand are more efficient—although not perfectly—in maintaining such slopes and therefore preserve the general shoaling properties in tsunami simulations (Kânoğlu & Synolakis 1998).

Contrary to moving average filters, decomposition methods are more promising as they are easily quantified (usually in the frequency domain), and since they are mathematically well-behaved functions, they preserve remaining bathymetric slopes, although not perfectly. Given the spherical nature of a tsunami environment, which cannot be neglected when considering propagation across an ocean basin, we will use the spherical harmonic expansion.

2 METHODOLOGY: DECOMPOSING THE BATHYMETRIC FIELD USING SPHERICAL HARMONICS

We recall that any given function F defined on a spherical surface (such as the field of actual topography/bathymetry at the Earth's surface) can be expanded onto a complete set of orthonormal spherical harmonic functions Y_l^m, representing eigenfunctions of Laplace's equation (e.g. Lee & Kaula 1967; Hirt & Rexer 2015):

$$F(\theta,\phi)=\sum_{l=0}^{\infty}\sum_{m=-l}^{l}a_{lm}Y_l^m(\theta,\phi), \tag{1}$$

where l and m are degree and order, respectively, θ and ϕ co-latitude and longitude and a_{lm} appropriate expansion coefficients. In this study, we express the Y_l^m using exponential harmonics: $Y_l^m = P_l^m(\cos\theta)\,e^{im\phi}$ $(-l \le m \le l)$, where P_l^m are Legendre associated functions of the first kind.

When applied to the elevation/bathymetry field, eq. (1) simply expresses that F can be reconstructed as the sum of its harmonic components, just like a 1-D function defined on a finite interval is the infinite but discrete sum of its spectral Fourier components. Of course, in real life the summation (1) has to be truncated at some maximum degree $l_{\max}$ controlling the physical resolution of the resulting bathymetry. While the most dominant features of the field are given by the first few terms of the expansion in eq. (1)—smaller l's or lower degrees—the smaller, more detailed features of the field require higher degrees (larger $l_{\max}$). In other words, the *resolution* of the resulting field is determined by the number of terms used from eq. (1). For example, in the case of the Earth with a circumference of ∼40 000 km, one can get to a physical resolution of ∼400 km by expanding the Earth's topography to the first 100 degrees ($l_{\max} = 100$).

In this study, in order to investigate the changes in the behaviour of tsunamis in bathymetry fields with various levels of physical resolution, we will focus on the Pacific bathymetry. This choice is based on the following reasons:

(i) The Pacific Ocean can be considered as a well-contained body of water (if not totally contained since it has a few free boundaries allowing flow through at its edges, for example, at the Drake passage and south of Australia), for which good bathymetry grids exist (e.g. Edwards 1989; National Geophysical Data Center 2006; IOC 2008; Amante & Eakins 2009).
While another choice with this property could have been the Indian Ocean, the average depths for the two oceans are similar (3868 and 3595 m, respectively), and we have verified that the slope distributions in both ocean basins have a correlation coefficient of 99 per cent, resulting from a trade-off between the slower spreading rates in the Indian Ocean which would lead to generally steeper slopes, and the greater number of passive margins (India, Africa, etc.) from which trenches, characterized by steep slopes, are absent. The similarity between the overall slope regime in the two basins can result in similar amplification of tsunami amplitudes during shoaling (Kânoğlu & Synolakis 1998).
As a result of these factors, the two oceans have similar hydrodynamic attributes, and the choice of one over the other in this study does not undermine the generality of our work.
(ii) Numerous earthquake tsunami sources in the Pacific have been the subjects of rigorous studies (e.g. Satake 1995; Satake *et al.* 1996; Titov & Synolakis 1997; Hébert *et al.* 2001; Okal *et al.* 2004; Synolakis & Okal 2005; López & Okal 2006; MacInnes *et al.* 2009; Fujii *et al.* 2011; Okal *et al.* 2011, 2014; Salaree & Okal 2018). As a result, we have a good understanding of the mechanisms and positions of tsunami sources in this basin. The Indian Ocean features only two margins with documented megathrust earthquakes: the Sumatra–Andaman and Makran trenches; the potential of the Java trench in this respect remains unresolved.
(iii) Finally, the Atlantic Ocean has virtually no subduction zones and was the site of only two quantitatively documented transoceanic tsunamis, the 1755 Lisbon event for which no consensus exists on a precise source location and mechanism (Baptista *et al.* 1998; Gutscher *et al.* 2002), and its 1761 sequel (Wronna *et al.* 2019).

Having selected the Pacific Basin for this study, we then use the ETOPO5 model grid (Edwards 1989) as a good approximation of the 'real' Pacific bathymetry. The choice of ETOPO5 rather than models with finer Res_s and Res_p, such as ETOPO1 and GEBCO, was made due to (i) the size of earthquake sources and therefore the dominant wavelength as prescribed in hydrodynamic models (e.g. Shuto *et al.* 1986; Titov & Synolakis 1995) and (ii) lower processing cost. A version of this model of the Pacific Ocean, compatible with our simulation routines, has been prepared and published by NOAA (Titov *et al.* 2016). The resolution of our grid (5 arcmin or ∼9 km at the Equator) compares favourably with typical ones used in transoceanic propagation (LeVeque *et al.* 2011; Gica *et al.* 2008), even though studies specifically targeted at the influence of dispersions have used finer ones (Kirby *et al.* 2013).

In Figs 1 and 2, we then expand the topography/bathymetry of the Pacific basin in spherical harmonics using increasingly large values of $l_{\max}$. Fig. 2 which shows the spectral power contained in each harmonic degree, documents that most of it is concentrated at lower degrees l.

A caveat in using this method to expand elevation fields is that contrary to 1-D Fourier expansion, the density of information at various latitudes is not uniform: as we approach either of the poles, higher latitudes have fewer physical details at smaller degrees. This simply expresses the fact that the area of Earth surface at colatitude θ decreases like $\sin\theta$ towards the poles.

Nevertheless, as the Arctic Ocean is largely isolated from the Pacific basin by continents north of 65°N, and continental Antarctica covers the southern latitudes beyond ∼70°S, this effect is expected to be marginal when expanding bathymetry for the purpose of our tsunami simulations, inherently limited to the Pacific basin.

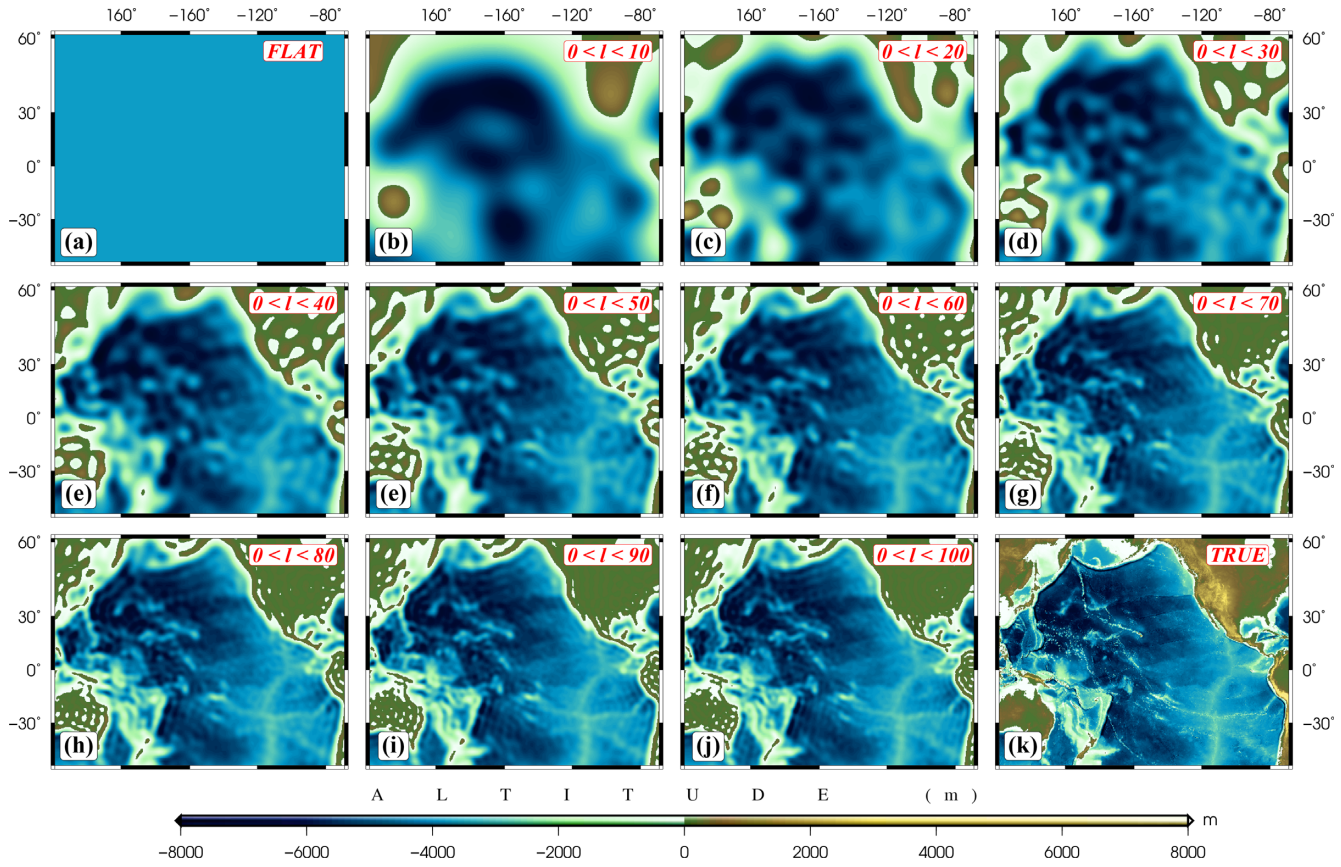

Figure 1. Expansion of the Pacific bathymetry using various values of maximum degree l_{max}.

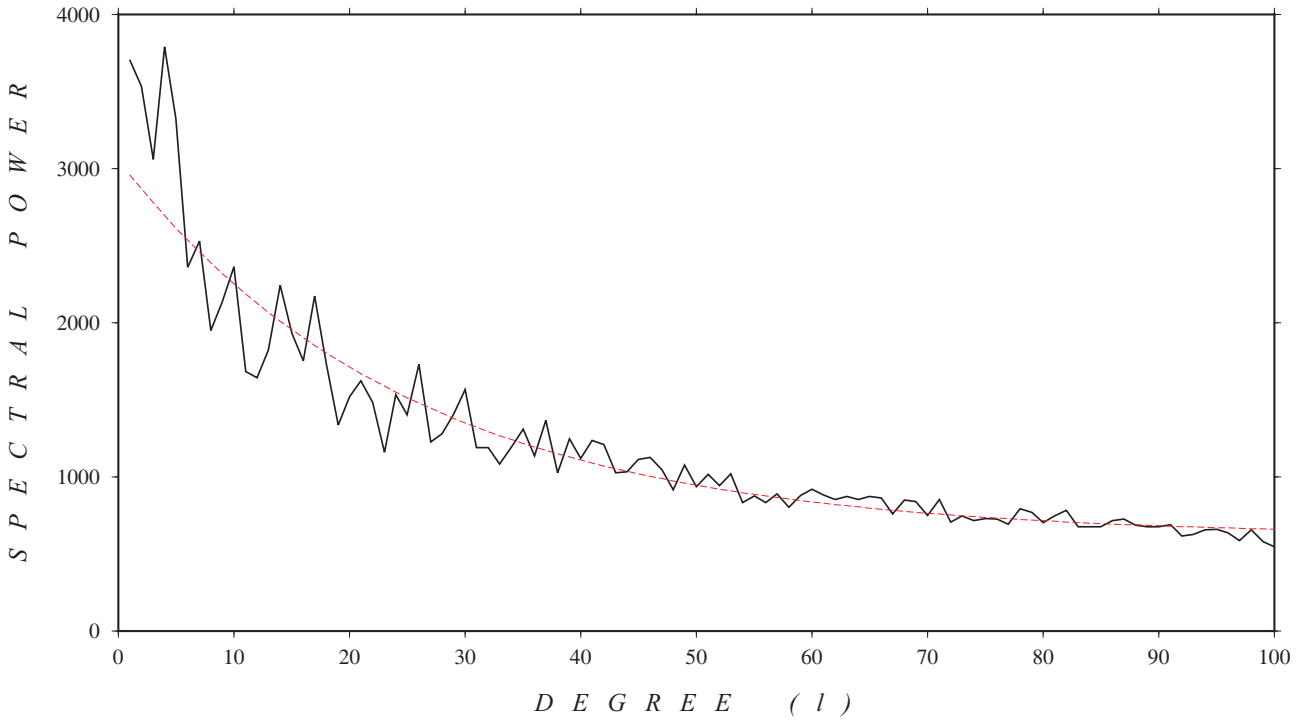

Figure 2. Distribution of spectral power over harmonic degree, with the dashed, red curve as a fit showing the general trend.

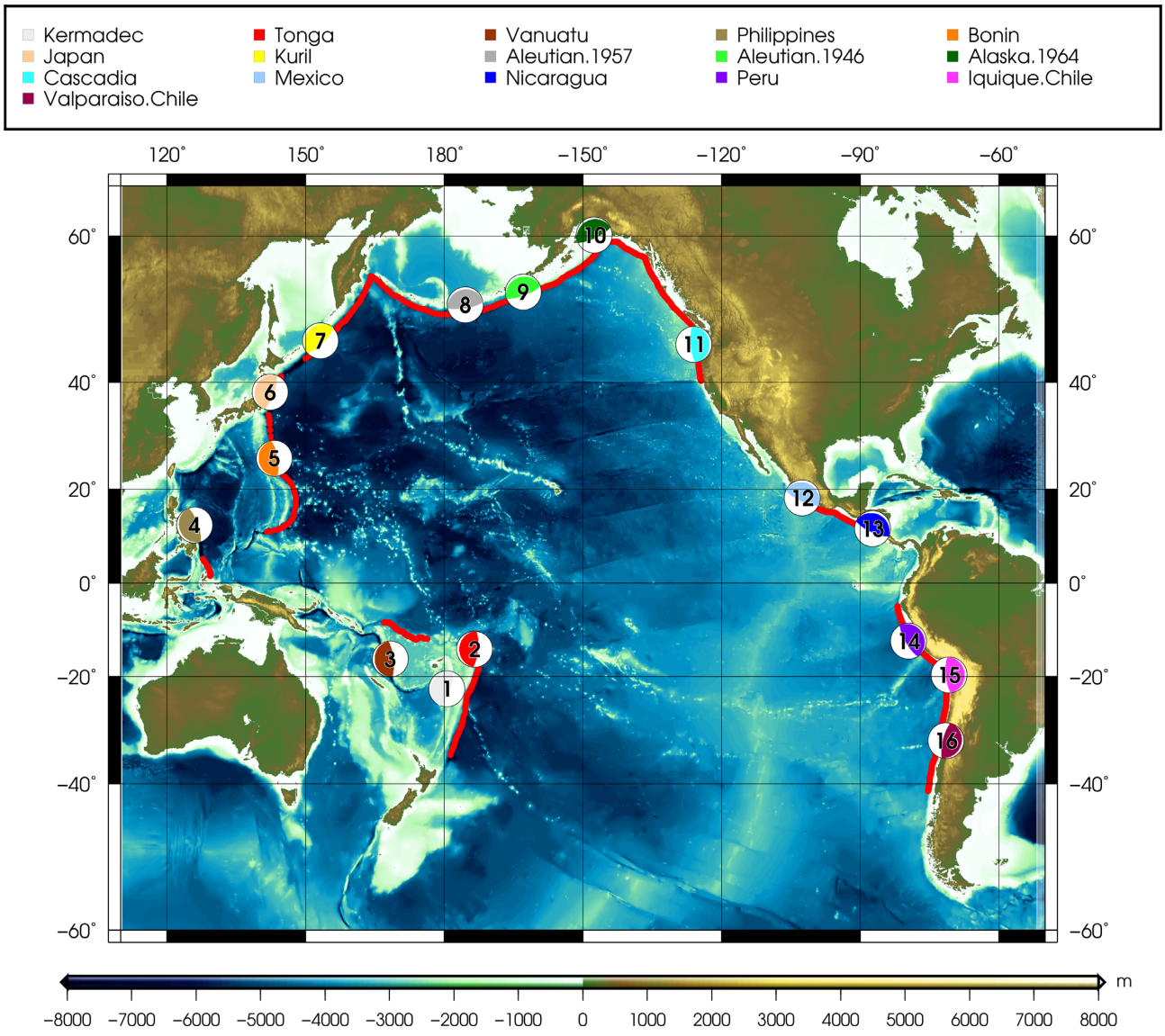

Figure 3. Seventeen designed tsunami sources around the Pacific. The strike angles of all the earthquake sources are chosen to follow those of their host trenches (red lines). Earthquakes are numbered according to Table 1.

3 TSUNAMI SOURCES

In order to avoid the influence of a particular source location on tsunami propagation, we selected 16 different locations around the Pacific margin mostly coinciding with those of previously studied events. This was done to constrain our study to realistic scenarios. We then considered pure shallow dipping thrust source mechanisms ($\delta = 15°$, $\lambda = 90°$) with strikes chosen along their host trenches, as shown in Fig. 3.

These epicentres are selected according to three criteria:

(i) All the trenches capable of creating large earthquakes are included.

(ii) Potential sources were chosen to create a good azimuthal coverage for the Pacific basin. This was done to accommodate the directivity effect for tsunamis (Ben-Menahem & Rosenman 1972), according to which tsunami waves from an earthquake interfere constructively in a direction perpendicular to the rupture.

(iii) Sources positioned at the epicentres of documented events, were extracted from either the publications addressing these events or the USGS catalogue, as listed in Table 1.

For all 16 designed sources, we calculated ocean floor deformation for three seismic moments of $M_0 = 10^{28}$, $M_0 = 10^{29}$, and $M_0 = 10^{30}$ dyn-cm (10^{21}, 10^{22} and 10^{23} N-m; $M_w = 7.9$, 8.6 and 9.3, respectively). This was done to avoid effects of a specific source size and therefore a particular dominant tsunami wavelength (e.g. Rabinovich 1997). All sources were placed with a depth of 10 km at the top of their rupture.

Note that the largest classes of moment may significantly exceed the level of known seismicity in the relevant subduction zone, specifically in Regions 3, 4 and 5 (Vanuatu, Philippines and Bonin-Mariana); however, in view of our lack of understanding of potential limitations on the size of interplate events (McCaffrey 2007; Stein & Okal 2007), our approach may be more than a purely didactic exercise. Similarly, the common focal geometry

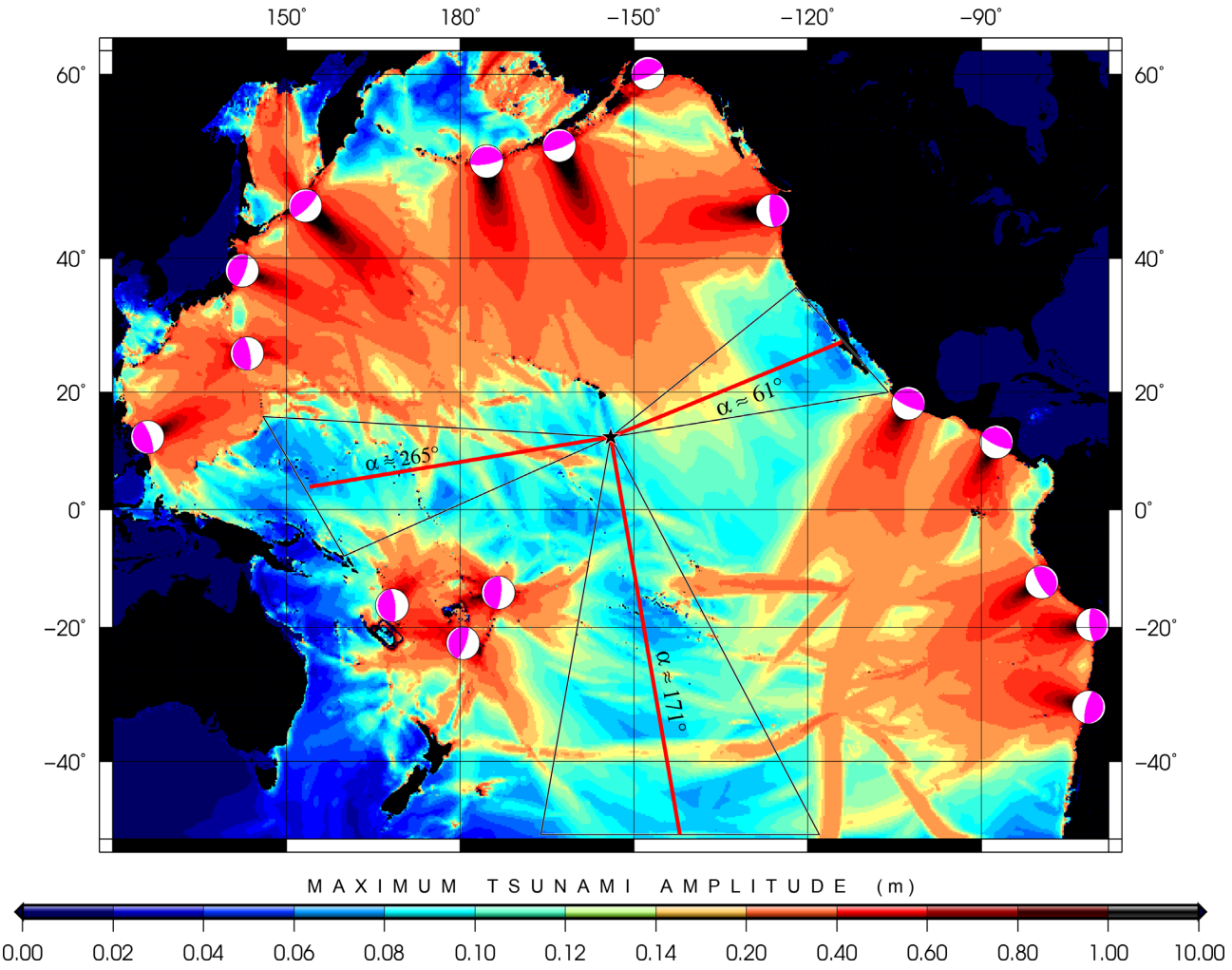

Figure 4. Maximum tsunami amplitudes from the 16 sources using earthquakes with seismic moments of $M_0 = 10^{29}$ dyn-cm in the real bathymetry field of the Pacific. The map is colour-coded according to tsunami amplitude in metres. The black star is the geometric centre of the simulation grid. The three black triangular sectors with a common corner at the geometric centre, illustrate the areas without significant maxima. The three red lines bisect the *star* corner of the sectors at the given azimuths α.

Table 1. Earthquake source data used for the 16 tsunami source scenarios.

No.	Location	Date	Lon.	Lat.	Strike (°)	Dip (°)	Slip (°)	Data source
1	Kermadec	1 May 1917	− 179.500	− 22.500	200	15	90	Okal *et al.* (2011)
2	Tonga	26 Jun 1917	− 173.400	− 14.250	185	15	90	USGS
3	Vanuatu	26 Nov 1999	168.210	− 16.420	174	15	90	CMT (Ekström *et al.* 2012)
4	Philippines	31 Oct 1975	125.999	12.537	160	15	90	Coffman & Stover (1984)
5	Bonin	7 Dec 1955	143.206	26.176	170	15	90	Okal *et al.* (2013)
6	Japan	11 Mar 2011	142.373	38.297	200	15	90	USGS
7	Kuril	15 Nov 2006	153.270	46.580	45	15	90	MacInnes *et al.* (2009)
8	Aleutian	9 Mar 1957	− 175.410	51.630	260	15	90	Johnson *et al.* (1994)
9	Aleutian	1 Apr 1946	− 162.880	53.310	250	15	90	López & Okal (2006)
10	Alaska	28 Mar 1964	− 147.600	61.100	245	15	90	Kanamori (1970)
11	Cascadia	26 Jan 1700	− 126.000	46.000	175	15	90	Satake *et al.* (2003)
12	Mexico	19 Sep 1985	− 102.530	18.190	295	15	90	USGS
13	Nicaragua	2 Sep 1992	− 87.386	11.727	295	15	90	Kanamori & Kikuchi (1993)
14	Peru-Chile	28 Oct 1746	− 77.780	− 12.390	330	15	90	Langer & Spence (1995)
15	Iquique, Chile	1 Apr 2014	− 70.770	− 19.610	355	15	90	USGS
16	Valparaiso, Chile	17 Aug 1906	− 71.400	− 32.400	15	15	90	Okal (2005)

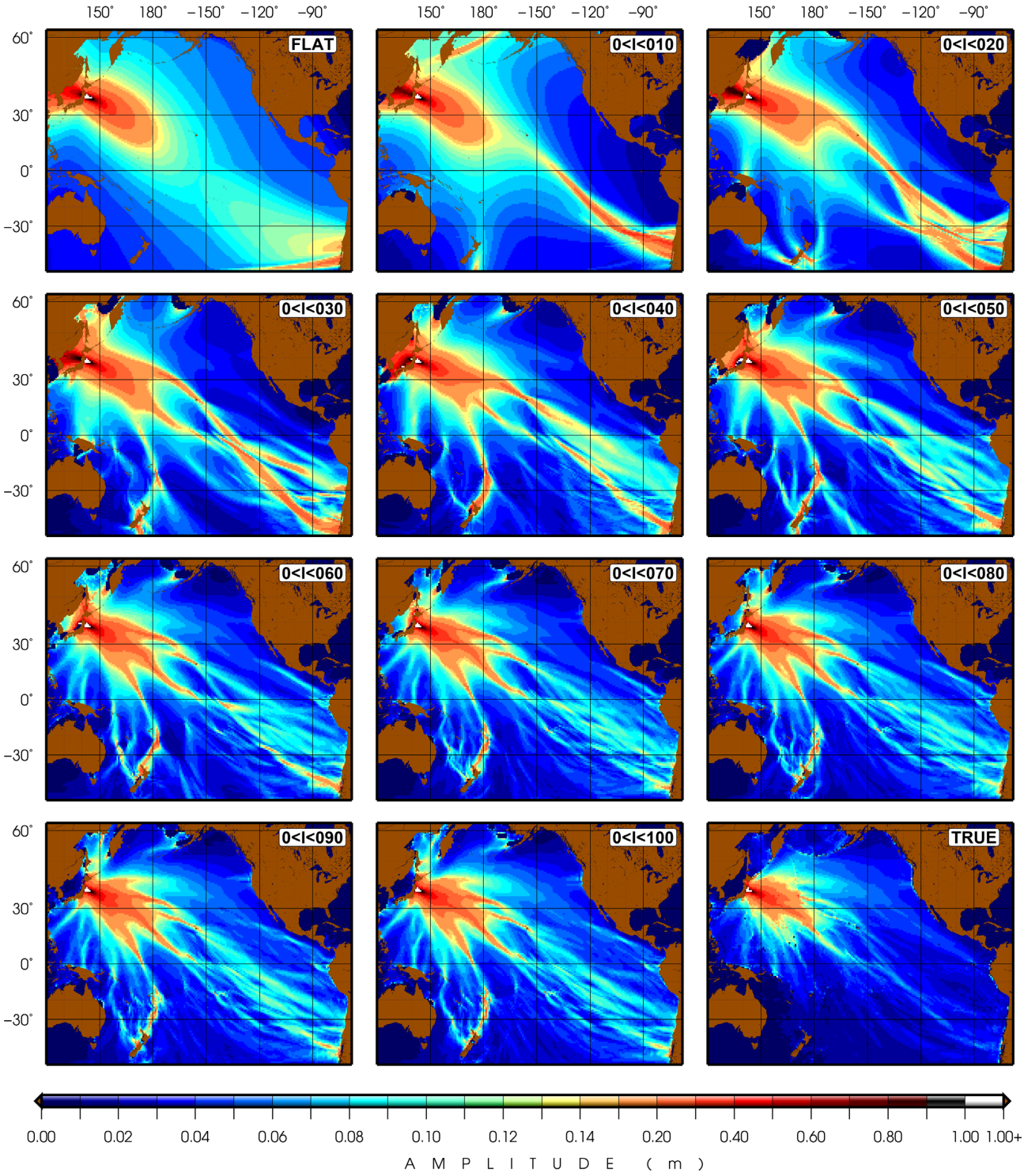

Figure 5. Maximum simulated tsunami amplitude in the Pacific for an earthquake in Japan, (number 6 in Table 1) with a seismic moment of $M_0 = 10^{29}$ dyn-cm.

($\delta = 15°$; $\lambda = 90°$) used in all these models may deviate from the actual mechanism of a historical earthquake of reference, as may the exact epicentres chosen for our simulations, all of which remain fundamentally of an experimental nature. For example, the largest known event in Region 4 (Philippines) has a normal faulting mechanism.

As mentioned above, the multitude of earthquake scenarios were chosen to obtain a more or less complete azimuthal coverage of tsunami maximum amplitudes throughout the Pacific. Fig. 4 shows the distribution of maximum amplitudes from all 16 sources, simulated in real bathymetry for a seismic moment of $M_0 = 10^{29}$ dyn-cm. The three triangular sectors in Fig. 4 isolate the areas without any

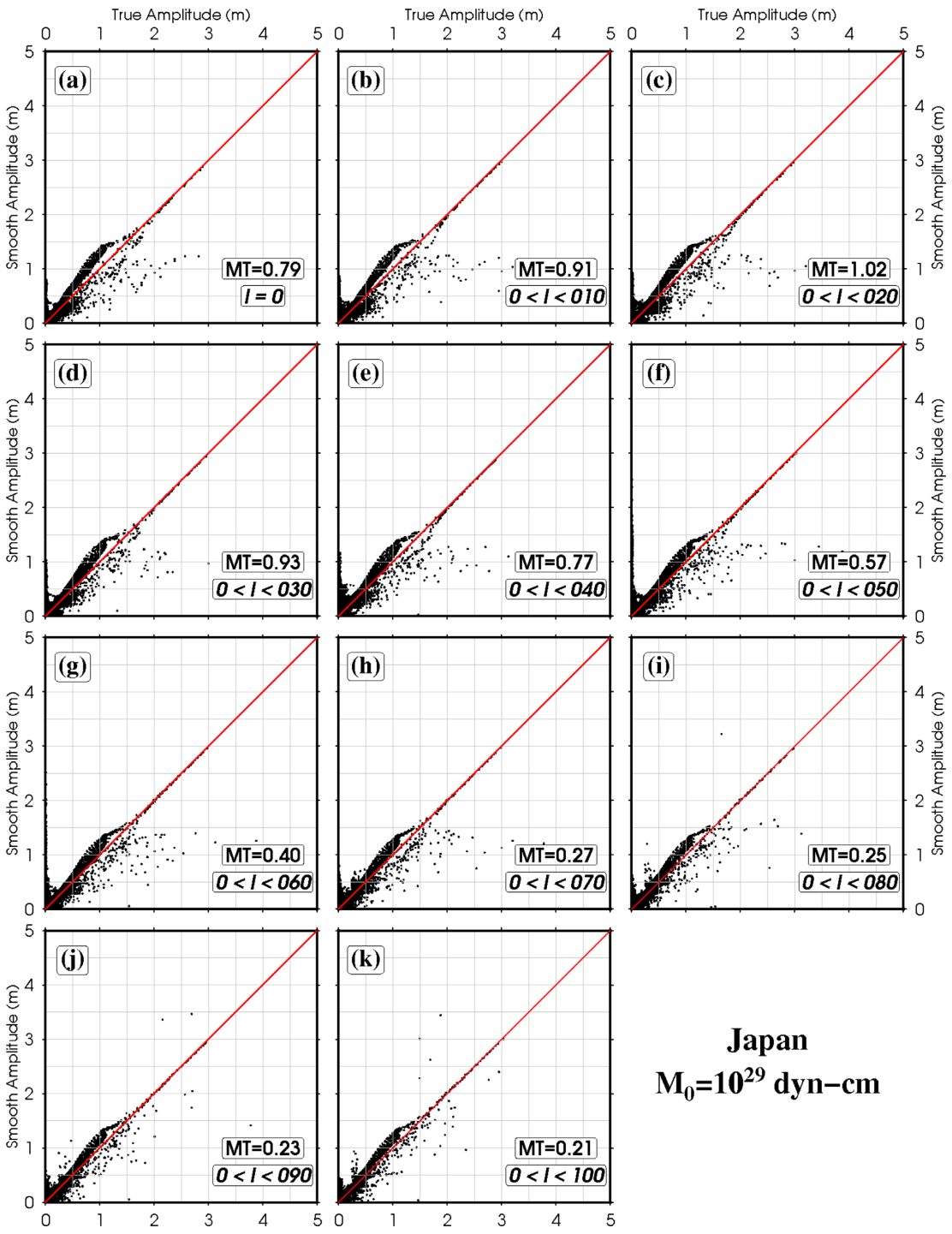

Figure 6. *MT* calculated for maximum tsunami amplitudes from a source near Japan (number 6 in Table 1) with $M_0 = 10^{29}$ dyn-cm, in various versions (l_{max}) of the Pacific bathymetry. The red line in all panels represents the perfect scenario where both amplitudes are equal for all grid points.

significant maxima. The red lines in this figure originate from the geometric centre (black star) of the map and bisect the common corner of the sectors, pointing toward the locations of non-existing sources that could cover the gaps—due to source directivity. This lack of coverage is due to the present plate tectonic pattern wherein the corresponding tectonic margins in Southwestern North America and Antarctica cannot host large tsunamigenic events, and the Northern Solomon-Caroline Sea area is not known to.

4 HYDRODYNAMIC SIMULATIONS

We have applied the Method of Splitting Tsunami or MOST algorithm (Titov *et al.* 2016) to calculate the propagation of tsunami waves from our hypothetical sources around the Pacific Ocean. MOST solves the shallow water approximation of the non-linear equations of hydrodynamics, using the method of alternate steps (Godunov 1959). It has been extensively validated through comparisons with laboratory and field data, per standard international

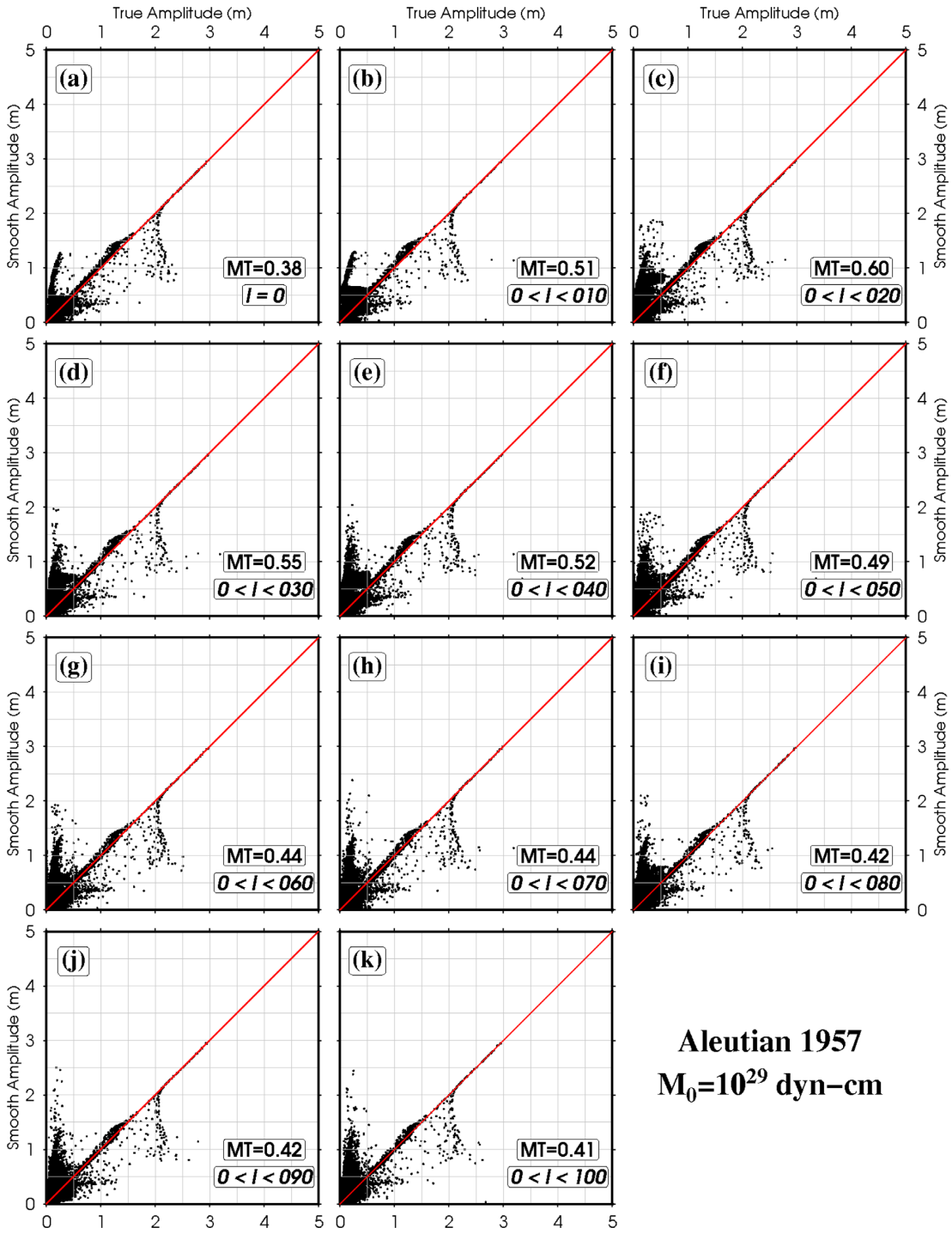

Figure 7. Similar to Fig. 6 for a source at the epicentre of the 1957 Aleutian earthquake (number 8 in Table 1).

protocols; full details can be found in Synolakis (2003) and Synolakis *et al.* (2008).

Since earthquake fault dimensions (primarily fault width), themselves controlled by seismic moment (Geller 1976), determine the dominant wavelength of the resulting tsunami (Rabinovich 1997), and following the general approach of Okal *et al.* (2014), we have simulated three seismic moment scenarios ($M_0 = 10^{28}$, $M_0 = 10^{29}$, $M_0 = 10^{30}$ dyn-cm, corresponding to fault lengths of $L \approx 110$, 240, 520 km) for each of the 16 earthquake locations.

However, an additional complexity emphasized by Okal *et al.* (2014) stems from the fact that a growth in fault length actually reduces the width of directivity lobes, as predicted theoretically by Ben-Menahem & Rosenman (1972), a result already discussed in the case of seismic, tsunami and air waves by Okal & Talandier (1991). As a consequence, the variation with source size of the sensitivity of tsunami amplitudes to higher degrees l of the bathymetry may not be predictable simply from arguments relating dominant wavelength to fault width.

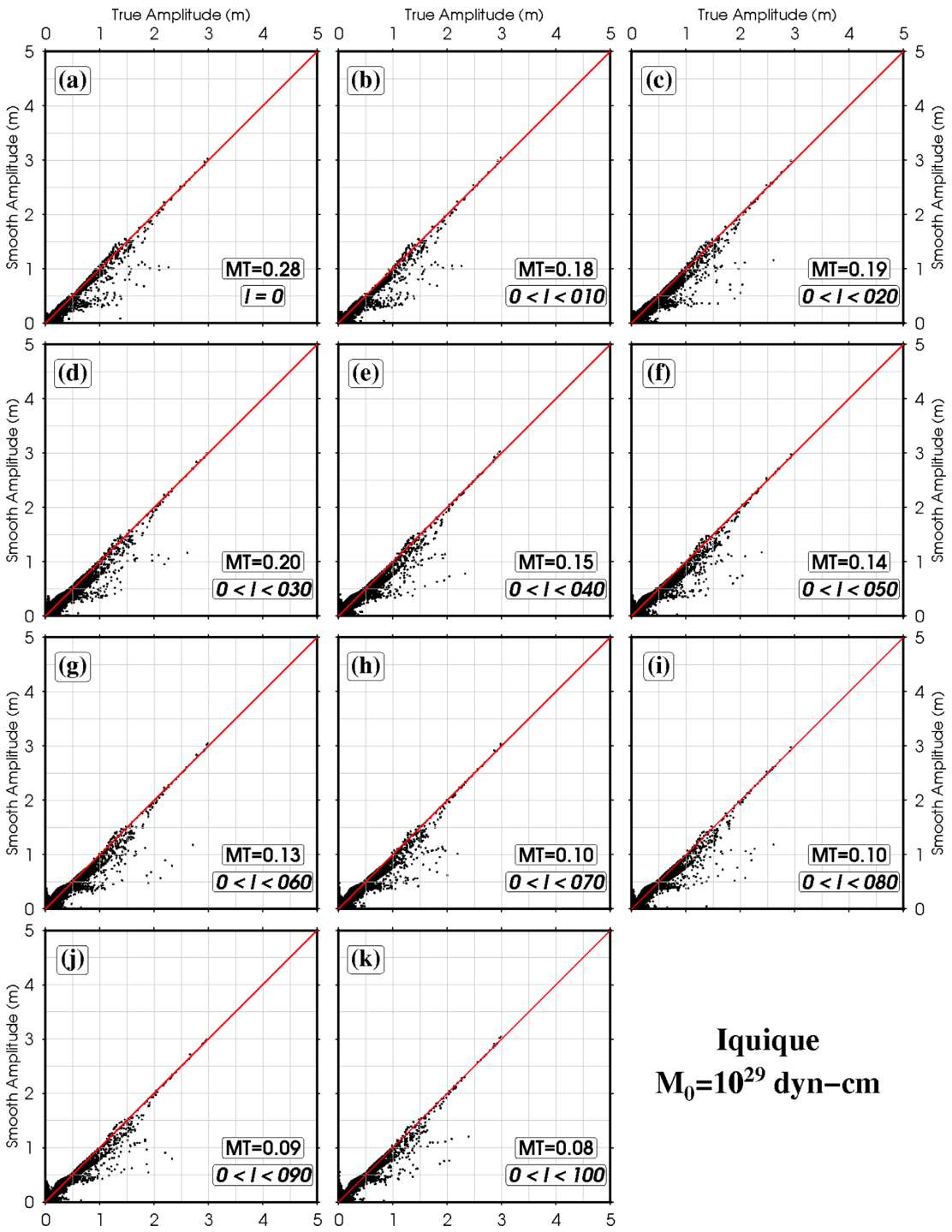

Figure 8. Similar to Fig. 6 for a source at the epicentre of the 2014 Iquique earthquake in Chile (number 15 in Table 1).

We then use Mansinha & Smylie's (1971) algorithm to calculate static deformation fields from earthquakes. This is done by assuming the proposed fault geometries (strike, dip and slip) in Table 1 (see Fig. 3). In this process, the fault dimensions, i.e. length and width are automatically calculated from moment using scaling relations for earthquake parameters as proposed by Geller (1976). While such scaling laws fail to invoke width (and possibly slip) saturation for the largest sources (Scholz 1982), we emphasize again that our primary goal here is to study the influence of the scale of bathymetric features on the amplitude of far-field tsunamis, rather than provide exact models of potential sources.

All simulations were performed for 24-hr time windows, allowing the tsunami to propagate throughout the entire Pacific Ocean. They were conducted using time steps of 10 s to satisfy the stability-resolution requirement (Courant *et al.* 1928) given our grid resolution (5 arcmin). Wave height calculations were truncated at a standard depth of 20 m along the coastlines to avoid nonlinear shoaling effects (e.g. Salaree & Okal 2015).

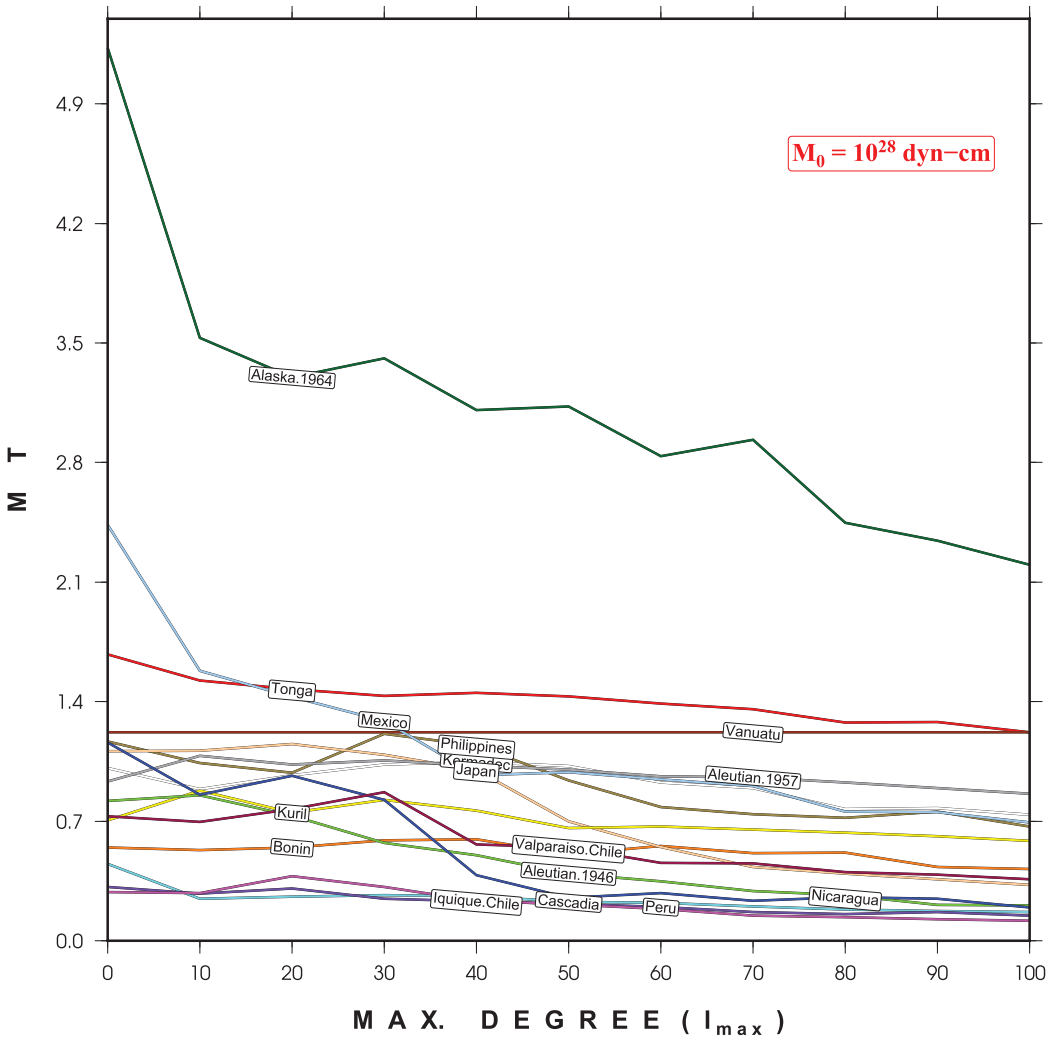

Figure 9. Calculated *MT* values for all earthquakes in Table 1 with a seismic moment of $M_0 = 10^{28}$ dyn-cm in various versions of the Pacific bathymetry created by choosing maximum spherical degrees (l_{max}). The curves are colour-coded according to the events in Fig. 3.

Tsunamis from each location–size scenario were simulated in bathymetries created by accumulating spherical degrees up to a maximum l_{max} varying in increments of 10 up to $l_{max} = 100$, that is, $l = 0$ (flat ocean floor), $0 \le l \le 10$, $0 \le l \le 20$, ..., $0 \le l \le 100$ and $l_{max} = \infty$ (true bathymetry). In the case of $l = 0$, we use the true average depth of the Pacific Ocean ($h_{mean} = 3868$ m) rather than the a_{00} coefficient of expansion of the combined bathymetry/topography, since the latter would strongly reduce the velocity of propagation of tsunamis across the basin. As a whole, a total of 612 scenarios were simulated and at the end of each simulation the fields of maximum tsunami amplitudes were recorded. The corresponding results for an example location, that is, Japan, 2011 (number 6 in Table 1) are shown for $M_0 = 10^{29}$ dyn-cm in Fig. 5.

5 ANALYSIS AND QUANTITATIVE METRIC *MT*

In very general terms, the 12 frames in Fig. 5 reveal expected patterns: for smoother bathymetries (flat or $l_{max} = 10$), the far-field amplitudes are controlled by the combination of source directivity (Ben-Menahem & Rosenman 1972), in this case beaming the tsunami energy in the azimuth N110° from the source, and geometrical spreading which would tend to eventually refocus the waves at the antipodes of the source. At intermediate l_{max}, significant focusing takes place along coherent shallow-depth features, but at large l_{max}, the effect of small scale bathymetry is generally that of a destructive interference (Okal *et al.* 2014) which in particular significantly affects the possibility of coherent refocusing for epicentral distances approaching 180°.

In the next sections, we study quantitatively the effects of bathymetric complexity (Res_p) on the tsunami propagation features by comparing the distributions of tsunami amplitudes for each level of complexity (as mapped for example in the various frames of Fig. 5), with that for the 'true' version, obtained using the full available details of bathymetry (last frame in Fig. 5).

In order to make a quantitative pointwise comparison between the tsunami amplitudes simulated under the true bathymetry (t_i) and under the smoothed one (s_i), we introduce the metric

$$MT(t,s) = \frac{\sum_{i=1}^{N}(s_i - t_i)^2}{\sum_{i=1}^{N} t_i^2} \qquad (2)$$

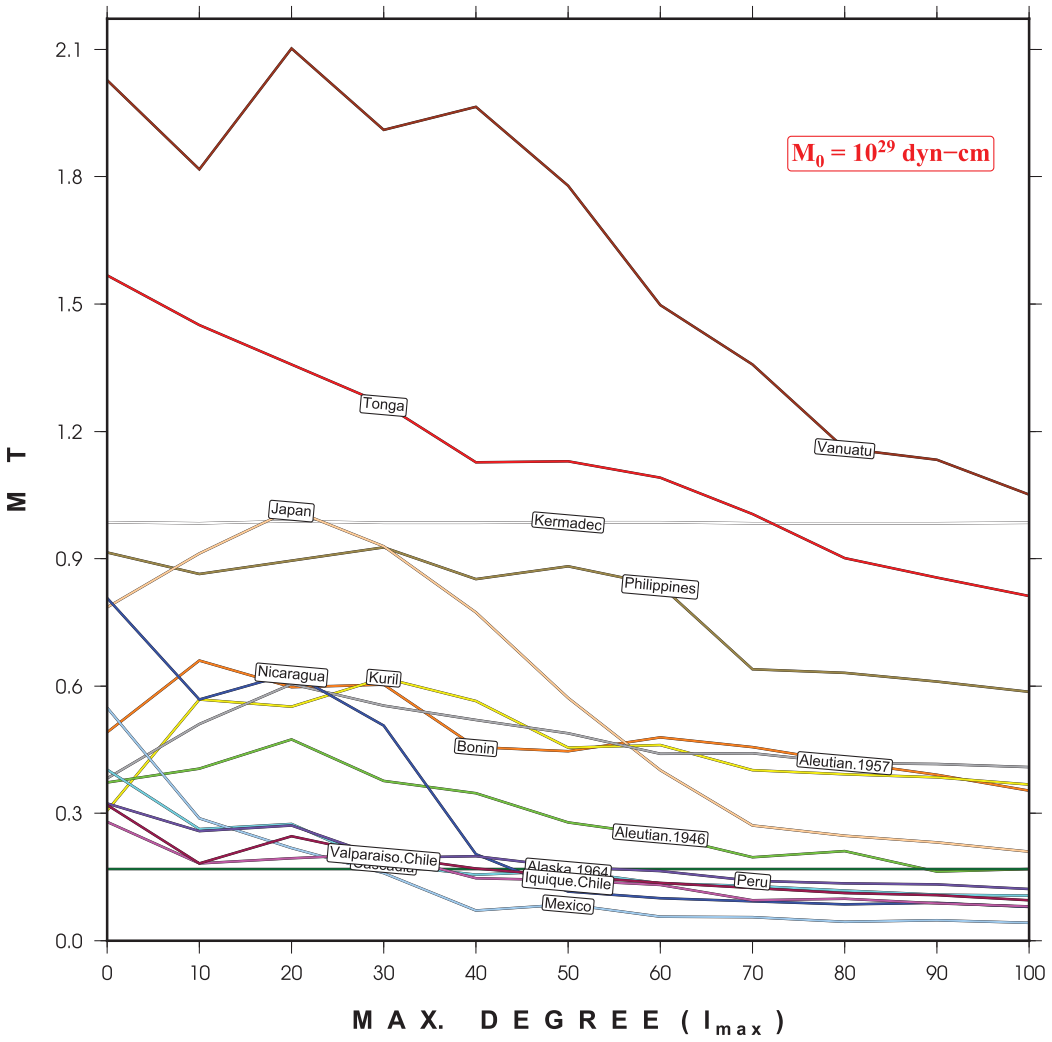

Figure 10. Calculated *MT* values for all earthquakes in Table 1 with a seismic moment of $M_0 = 10^{29}$ dyn-cm in various versions of the Pacific bathymetry created by choosing maximum spherical degrees (l_{max}). The curves are colour-coded according to the events in Fig. 3. Note the different ordinate scale from Fig. 9.

which is a dimensionless variant of the mean square residual between two fields, with smaller values of *MT* corresponding to smaller misfits, and consequently to a better performance of the smoothed field. A similar apprioach was used by Stein *et al.* (2015) to compare observed and predicted seismic intensities in order to quantify how well a given model can predict spatial variations in shaking (Brooks *et al.* 2018).

In Figs 6–8 we compare, for various l_{max}, maximum tsunami amplitudes at each point of the simulation grid, computed under the true and smoothed bathymetries, in the case of an intermediate-size seismic source ($M_0 = 10^{29}$ dyn-cm) located near Japan (number 6 in Table 1; Fig. 6), Aleutians (number 8; Fig. 7) and Northern Chile (number 15; Fig. 8).

In general terms and expectedly, the fit improves (and hence *MT* decreases) when l_{max} is increased, as shown in Figs 9 to 11. In addition, these figures (which have different ordinate scales) show that the metric *MT* is generally greater for smaller sources, which are richer in higher frequencies, and hence more sensitive to finer bathymetry.

We also note that, in general and especially at low l_{max}, the smoothed amplitudes are slightly larger than the ones under the true bathymetry. As noted by Okal *et al.* (2014), irregular bathymetry will focus or defocus tsunami rays, but focusing by a lens is limited to the vicinity of its focus, with rays eventually diverging beyond it, so that on the large scale of a basin, the effect of irregular bathymetry is generally to defocus tsunami energy, as observed on Fig. 6, especially at high l_{max}.

This remark may also explain the occasional irregular behaviour of *MT* with l_{max}. For example, in the case of the intermediate source in Japan, *MT* grows from $l_{max} = 0$ to 20, before decreasing regularly for $l_{max} > 20$ (Fig. 10). This can be explained by the presence of long-wavelength features such as the Hawaiian chain and the East Pacific Rise, strongly expressed at $l_{max} = 20$, and acting as lens potentially increasing the effect of refocusing by geometrical spreading in the Southeast Pacific. However, this effect is largely canceled at shorter wavelengths, and hence using the true bathymetry, which can explain a maximum value of *MT* for $l_{max} = 20$ in this particular geometry.

An interesting feature of Fig. 6 is a small population of large amplitudes obtained in the true bathymetry model to the lower right of the red line, i.e., not reproduced in the smoothed models, at least for $l_{max} \leq 60$. We have verified that these points are located close to the source, on either side of the Japan trench. At low values of l_{max}, the difference in water depth between source (deep) and receiver

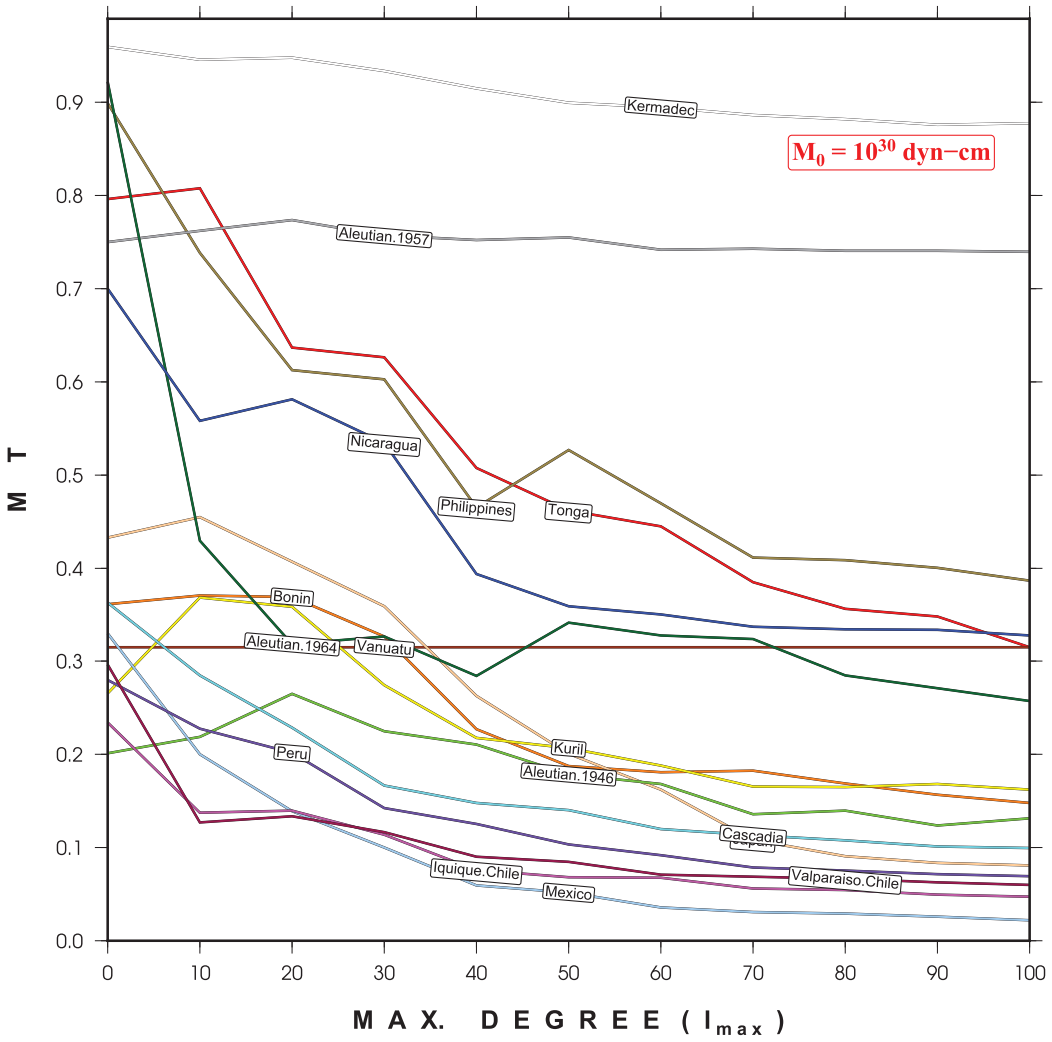

Figure 11. Calculated *MT* values for all earthquakes in Table 1 with a seismic moment of $M_0 = 10^{30}$ dyn-cm in various versions of the Pacific bathymetry created by choosing maximum spherical degrees (l_{max}). The curves are colour-coded according to the events in Fig. 3. Note the different ordinate scale from Fig. 9.

(shallow), which will increase amplitude at these receivers under Green's law (Kirby 1991; Synolakis 1991), is smoothed out and thus the amplification at these points is not modeled.

In the case of the Aleutian 1957 source (Fig. 7), the metric *MT* remains much more stable, and the points in the vicinity of the source remain poorly fit even at $l_{max} = 100$, which could reflect a trench bathymetry of higher spatial frequency. The group of points to the left of the red line with much larger amplitudes under the smooth bathymetry correspond to propagation into the Bering Sea behind the Aleutian arc, obviously a significant barrier in the true model, but smoothed out, even for large values of l_{max}. The absence of the Aleutian arc was largely irrelevant for the Japanese source since the tsunami was beamed at right angle to it, and the amplitude when reaching the arc was already small in the smoothed models. As for the Northern Chile (Iquique 2014) scenario (Fig. 8), it shows very low values of *MT*, practically independent of l_{max}. This may be due to the much shallower trench and poorly developed continental shelf, which will minimize the effect of Green's law in this highly coupled subduction zone (Uyeda & Kanamori 1979).

Finally, we note on Figs 9 to 11 that the Vanuatu and Alaska (1964) scenarios generally feature anomalous values of *MT*, especially for low values of l_{max}. We have documented that the locations contributing to this scatter are mostly situated in the immediate vicinity of the sources. For example, in the case of Alaska, they lie inside the numerous islets located in the back of the Alaska Peninsula, which disappear at low l_{max}, or on the extensive continental shelf present in the Gulf of Alaska.

The case of Vanuatu for which the metric remains high at intermediate moments even for high l_{max}, is examined in detail on Fig. 12. As shown on frame (a), the true bathymetry in the source area is very complex, featuring several islands of different sizes (e.g. Espiritu Santo), the relatively narrow d'Entrecasteaux Ridge, as well as subduction behind an active backarc system (the Fiji plateau) characterized by shallow and irregular bathymetry. As a result, even for $l_{max} = 100$, the smoothed bathymetry differs significantly from the true one in the source area (frame (b)), which will affect the simulations. By contrast, in the case of Japan, frames (c) and (d) show a much improved bathymetric fit at $l_{max} = 100$, with the result that the simulations are more consistent and the Metric *MT* is lower.

We further interpret Figs 9–11 as follows:

For each of the three moments considered, and for each value of l_{max}, we average the values of *MT* over all epicentral regions

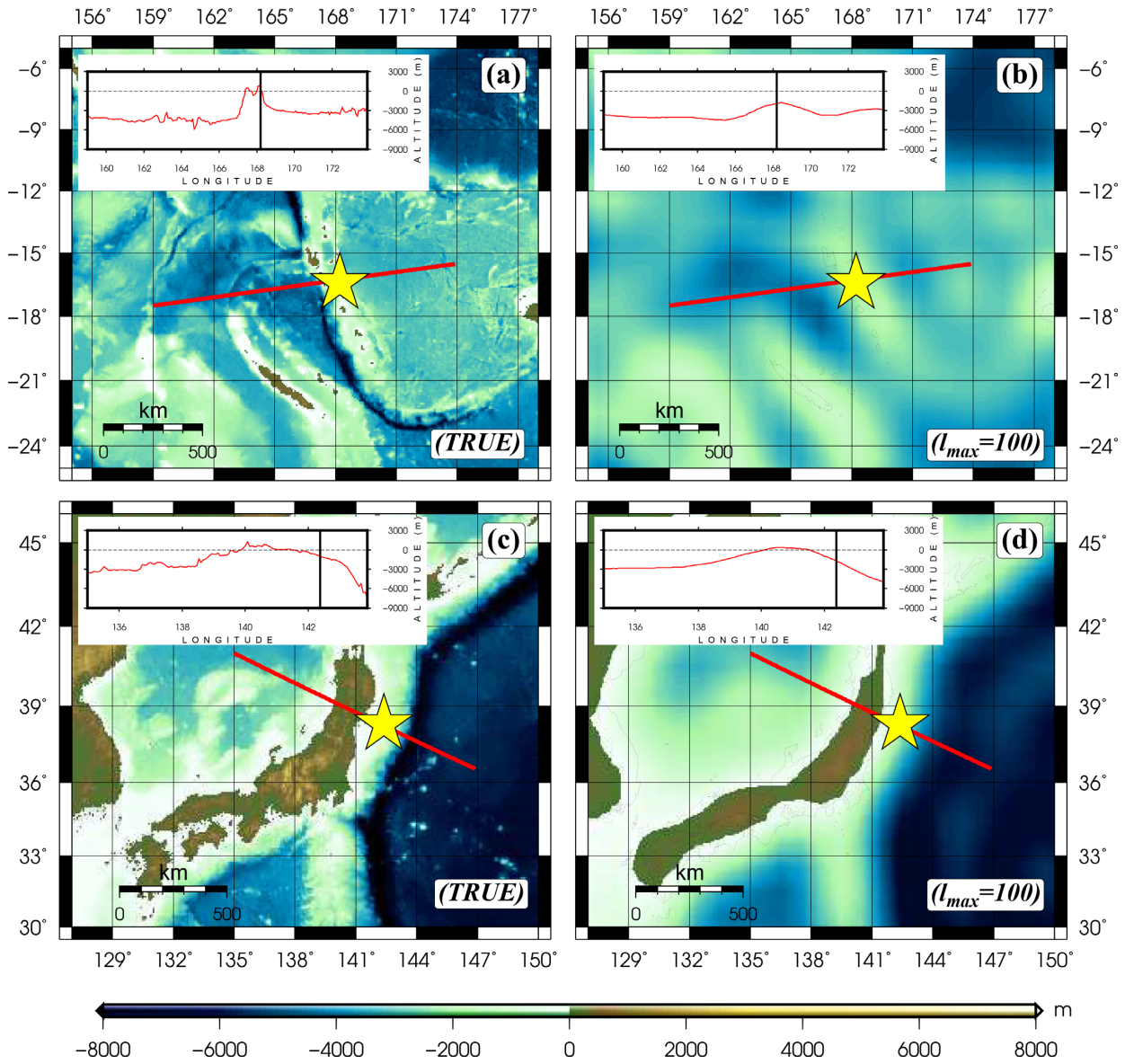

Figure 12. (a) True and (b) smoothed ($l_{\max} = 100$) bathymetry of Vanuatu (number 3 in Table 1). The smaller panels on the top-left corners of (a) and (b) show bathymetry cross sections along the red lines in the main panel; the yellow stars represent the epicentre used for Vanuatu in this study . (c) True and (d) smoothed ($l_{\max} = 100$) bathymetry of Japan (number 6 in Table 1) annotated similar to (a) and (b).

(excluding clear outliers such as Vanuatu and Alaska on Fig. 10). To make the data comparable between the three moments, we divide the result by a factor of 2 for $M_0 = 10^{28}$ dyn-cm, $\frac{4}{3}$ for $M_0 = 10^{29}$ dyn-cm and $\frac{2}{3}$ for 10^{30} dyn-cm, respectively, which are gross estimates of the maximum value of MT for that moment range. The three resulting data sets are plotted on Fig. 13(a) and give, for each moment level, an estimate of the evolution of the goodness of fit of the data set of simulations s_i to that of the true maximum amplitudes t_i, as the parameter $l_{\max}$ is increased, averaged over all source areas to eliminate specific cases, as described above in the case of the intermediate moment source in Japan.

It is clear from Fig. 13(a) that for the largest moment, $M_0 = 10^{30}$ dyn-cm, the effect of smoothing slows down considerably for $l_{\max} \geq 40$, whereas no such trend is detectable at the lower moments. This is confirmed by applying an F-test to the regression of the three data sets of scaled average MT values as one or two segments. This classical method introduced by Snedecor & Cochran (1937) has been applied to geophysical data, e.g., by Stein & Gordon (1984). For the largest moment, Fig. 13(b) shows F-test values in excess of four times $F_{1\,\text{per cent}}$ and eight times $F_{5\,\text{per cent}}$ as compiled by Dixon & Massey (1950), which means that the elbow in the distribution is significant even at the 99 per cent confidence level; by contrast, the data sets for the other two moments fail the F-test, even at the lower 95 per cent level.

We interpret this result as meaning that, for the largest sources, maximum tsunami amplitudes are most sensitive to bathymetric features with wavelengths greater than 1000 km, which not surprisingly, corresponds to approximately two fault lengths, or under common scaling laws (Geller 1976), four fault widths, the latter known to control the dominant wavelengths of the tsunami (Rabi-

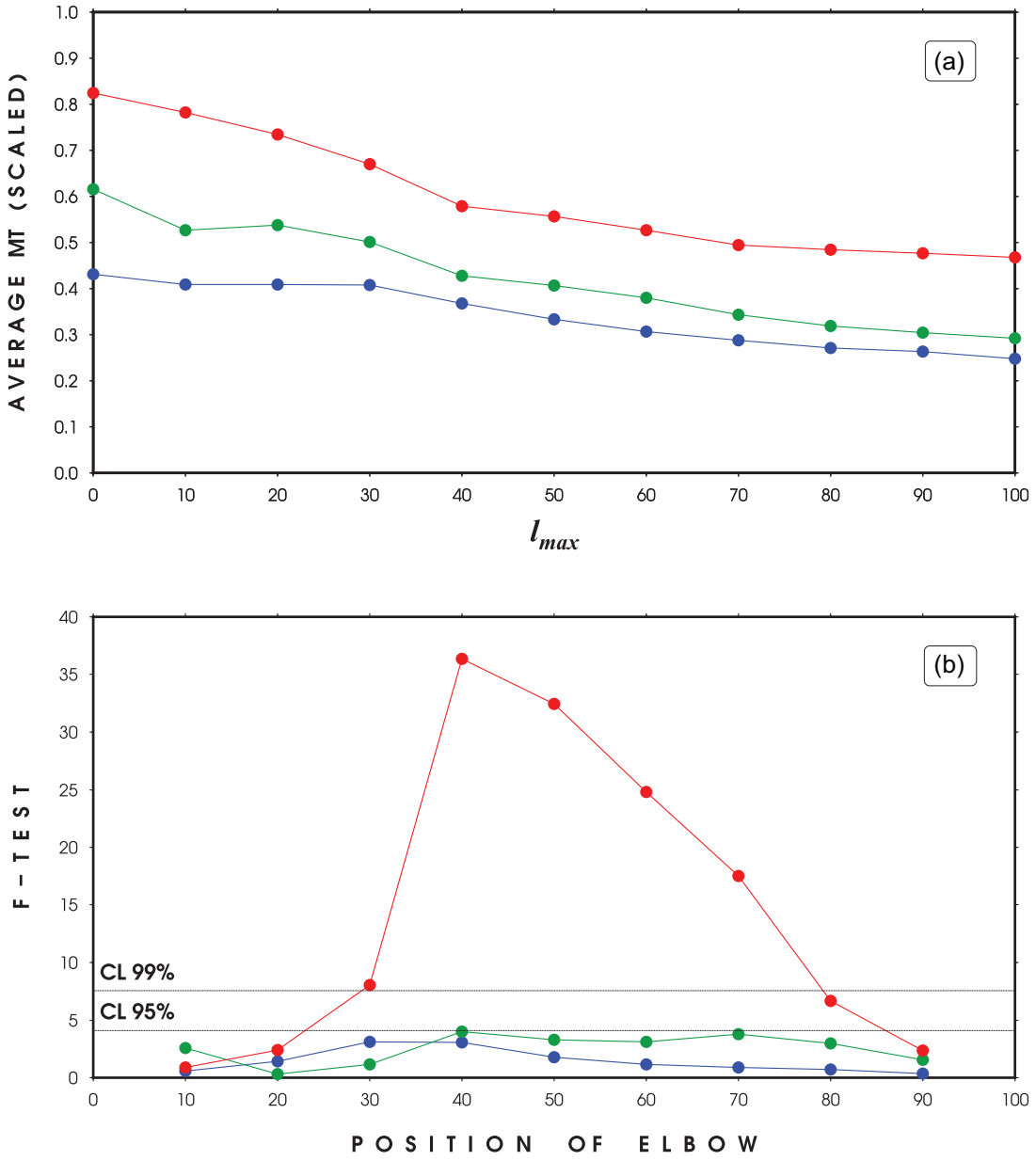

Figure 13. (a) Metric *MT* averaged over source as a function of l_{max} for the three moment levels (10^{28} dyn-cm, blue; 10^{29} dyn-cm, green; 10^{30} dyn-cm, red). (b) F-test applied to the data sets in (a) rearranged as single vs. double segment as a function of the position *l*, of the elbow between the segments. Note that only the 10^{30} dyn-cm data set passes the F-test at the 99 per cent and 95 per cent confidence levels (CL).

novich 1997). Tsunamis from smaller sources would be expected to be sensitive to higher l_{max}; however, our data sets cannot resolve comparable elbows.

6 CONCLUSIONS

In this study, we investigated the effects of physical resolution of bathymetry (Res_p) on the distribution of maximum tsunami amplitudes in the Pacific Ocean as a semi-closed, well-studied basin. In order to resolve the physical complexity or resolution of the Pacific, we decomposed the bathymetry using spherical harmonics.

We used a total of 48 seismic sources, spread over 16 regions and three levels of seismic moment, and simulated their tsunamis throughout the Pacific Basin using bathymetric grids smoothed at 12 different levels of spherical harmonic approximations, including a totally flat ocean floor and the actual ('true') ETOPO5 bathymetry.

For each value l_{max} of the maximum degree of spherical harmonic expansion of the bathymetry, and for each focal geometry, we use a metric *MT* to compare the maximum amplitude of the resulting tsunami at each simulation grid point to its value obtained under the full ETOPO5 bathymetry. For the largest sources ($M_0 = 10^{30}$ dyn-cm), and averaging over all source locations, the *MT* metric suggests a change of behaviour at $l_{max} = 40$ (~1000 km), a level at which bathymetric Res_p is sufficient to reproduce the main features of the tsunami, as confirmed at the 99 per cent confidence level by applying an *F*-test to the regression of the data set of scaled average *MT* values as one or two segments. We interpret this result as meaning that, for the largest sources, maximum tsunami amplitudes are most sensitive to bathymetric features with wavelengths greater than 1000 km,

in agreement with common scaling laws (Geller 1976) governing the growth of fault width, this parameter controlling the dominant wavelengths of the tsunami (Rabinovich 1997).

By contrast, at smaller moments ($M_0 = 10^{28}$ and 10^{20} dyn-cm), our *F*-tests fail to identify a definitive elbow (Fig. 13) and the metric *MT* keeps decreasing regularly with increasing l_{max}, at least in the domain considered here ($l_{max} \leq 100$). This illustrates the fact that shorter dominant wavelengths of the tsunamis excited by such smaller sources remain more sensitive to fine scale bathymetry, which expand at higher degrees of spherical harmonics.

Based on this analysis, threshold l_{max} values for $M_0 = 10^{29}$ and 10^{28} dyn-cm should be around $l_{max} \approx 85$ and $l_{max} \approx 180$, respectively. While using grids with very high Res_p will produce the most accurate tsunami simulations, and noting the fact that the desired resolution in these simulations depends on the scale of any study, our results suggest that the most dominant features of far-field tsunami propagation in deep water can be achieved using a physical resolution twice as fine as the earthquake source size.

ACKNOWLEDGEMENTS

We are grateful to David Sandwell for spherical harmonics software, and to Costas Synolakis for discussion. This study constituted a chapter of the first author's Doctoral dissertation at Northwestern University, where he was partially supported by a subcontract from the University of Pittsburgh under National Science Foundation Grant Number OCE-13-31463. The final preparation of this manuscript was supported by the University of Michigan. We thank Frédéric Dias, another, anonymous reviewer and Editor Duncan Agnew for their constructive comments on the original version of the manuscript. Some figures were drafted using the Generic Mapping Tools (Wessel & Smith 1991).

REFERENCES

Amante, C. & Eakins, B.W., 2009, ETOPO1 1 arc-minute global relief model: procedures, data sources and analysis, US Department of Commerce, National Oceanic and Atmospheric Administration, National Environmental Satellite, Data, and Information Service, National Geophysical Data Center, Marine Geology and Geophysics Division, Boulder, Colorado.

AMS, 2015. Weather analysis and forecasting, Statements of the American Meteorological Society in Force.

Baptista, M., Miranda, P., Miranda, J. & Victor, L.M., 1998. Constraints on the source of the 1755 Lisbon tsunami inferred from numerical modelling of historical data on the source of the 1755 Lisbon tsunami, *J. Geodyn.,* **25**(1–2), 159–174.

Becker, J., *et al.*, 2009. Global bathymetry and elevation data at 30 arc seconds resolution: SRTM30_PLUS, *Mar. Geod.,* **32**(4), 355–371.

Ben-Menahem, A. & Rosenman, M., 1972. Amplitude patterns of tsunami waves from submarine earthquakes, *J. geophys. Res.,* **77**(17), 3097–3128.

Brooks, E.M., Stein, S., Spencer, B.D., Salditch, L., Petersen, M.D. & McNamara, D.E., 2018. Assessing earthquake hazard map performance for natural and induced seismicity in the Central and Eastern United States, *Seismo. Res. Lett.,* **89**(1), 118–126.

Coffman, J.L. & Stover, C.W., 1984. United States Earthquakes, 1975, U.S. Geological Survey (Open-File report 84-975).

Courant, R., Friedrichs, K. & Lewy, H., 1928. Über die partiellen Differenzengleichungen der mathematischen Physik, *Math. Ann.,* **100**(1), 32–74.

Dixon, W.J. & Massey, F.J., 1950. *Introduction To Statistical Analysis,* McGraw-Hill Book Company, Inc.

Edwards, M., 1989. Global gridded elevation and bathymetry on 5-minute geographic grid (ETOPO5), NOAA, National Geophysical Data Center, Boulder, Colorado, USA.

Ekström, G., Nettles, M. & Dziewoński, A., 2012. The global CMT project 2004–2010: centroid-moment tensors for 13,017 earthquakes, *Phys. Earth planet. Inter.,* **200,** 1–9.

Fujii, Y., Satake, K., Sakai, S., Shinohara, M. & Kanazawa, T., 2011. Tsunami source of the 2011 Off the Pacific coast of Tohoku earthquake, *Earth, Planets Space,* **63**(7), 55.

Geller, R.J., 1976. Scaling relations for earthquake source parameters and magnitudes, *Bull. seism. Soc. Am.,* **66**(5), 1501–1523.

Gica, E., Spillane, M.C., Titov, V.V., Chamberlin, C.D. & Newman, J.C., 2008. Development of the forecast propagation database for NOAA's short-term inundation forecast for tsunamis (SIFT), NOAA Tech. Memo. OAR PMEL–139.

Godunov, S.K., 1959. Finite difference method for numerical calculation of discontinuous solutions of the equations of hydrodynamics, *Matemat. Sbornik,* **47,** 271–295.

Gutscher, M.-A., Malod, J., Rehault, J.-P., Contrucci, I., Klingelhoefer, F., Mendes-Victor, L. & Spakman, W., 2002. Evidence for active subduction beneath Gibraltar, *Geology,* **30**(12), 1071–1074.

Hébert, H., Heinrich, P., Schindelé, F. & Piatanesi, A., 2001. Far-field simulation of tsunami propagation in the Pacific Ocean: impact on the Marquesas Islands (French Polynesia), *J. geophys. Res.,* **106**(C5), 9161–9177.

Hirt, C. & Rexer, M., 2015. EARTH2014: 1 arc-min shape, topography, bedrock and ice-sheet models–available as gridded data and degree-10,800 spherical harmonics, *International J. Appl. Earth Obser. Geoinform.,* **39,** 103–112.

IOC, 2008. BODC: centenary edition of the GEBCO Digital Atlas, published on cd-rom on behalf of the Intergovernmental Oceanographic Commission and the International Hydrographic Organization as part of the General Bathymetric Chart of the Oceans, British Oceanographic Data Centre, Liverpool, UK, 260 pp.

Johnson, J.M., Tanioka, Y., Ruff, L.J., Satake, K., Kanamori, H. & Sykes, L.R., 1994. The 1957 great Aleutian earthquake, *Pure appl. Geophys.,* **142**(1), 3–28.

Kanamori, H., 1970. The Alaska earthquake of 1964: Radiation of long-period surface waves and source mechanism, *J. geophys. Res.,* **75**(26), 5029–5040.

Kanamori, H. & Kikuchi, M., 1993. The 1992 Nicaragua earthquake: a slow tsunami earthquake associated with subducted sediments, *Nature,* **361**(6414), 714.

Kânoğlu, U. & Synolakis, C.E., 1998. Long wave runup on piecewise linear topographies, *J. Fluid Mech.,* **374,** 1–28.

Kirby, J.T., 1991. Intercomparison of truncated series solutions for shallow water waves, *J. Waterway, Port, Coastal, Ocean Eng.,* **117**(2), 143–155.

Kirby, J.T., Shi, F., Tehranirad, B., Harris, J.C. & Grilli, S.T., 2013. Dispersive tsunami waves in the ocean: Model equations and sensitivity to dispersion and Coriolis effects, *Ocean Modell.,* **62,** 39–55.

Langer, C. & Spence, W., 1995. The 1974 Peru earthquake series, *Bull. seism. Soc. Am.,* **85**(3), 665–687.

Lee, W. & Kaula, W., 1967. A spherical harmonic analysis of the Earth's topography, *J. geophys. Res.,* **72**(2), 753–758.

LeVeque, R.J., George, D.L. & Berger, M.J., 2011. Tsunami modelling with adaptively refined finite volume methods, *Acta Numer.,* **20,** 211–289.

López, A.M. & Okal, E.A., 2006. A seismological reassessment of the source of the 1946 Aleutian "tsunami" earthquake, *Geophys. J. Int.,* **165**(3), 835–849.

MacInnes, B.T., Pinegina, T.K., Bourgeois, J., Razhigaeva, N.G., Kaistrenko, V.M. & Kravchunovskaya, E.A., 2009. Field survey and geological effects of the 15 November 2006 Kuril tsunami in the middle Kuril Islands, *Pure appl. Geophys.,* **166,** 9–36.

Mansinha, L. & Smylie, D., 1971. The displacement fields of inclined faults, *Bull. seism. Soc. Am.,* **61**(5), 1433–1440.

McCaffrey, R., 2007. The next great earthquake, *Science,* **315**(5819), 1675–1676.

National Geophysical Data Center, 2006. 2-minute gridded global relief data (ETOPO2v2).

Okal, E.A., 2005. A re-evaluation of the great Aleutian and Chilean earthquakes of 1906 August 17, *Geophys. J. Int.,* **161**(2), 268–282.

Okal, E.A. & Talandier, J., 1991. Single-station estimates of the seismic moment of the 1960 Chilean and 1964 Alaskan earthquakes, using the mantle magnitude M_m, *Pure appl. Geophys.,* **136**(1), 103–126.

Okal, E.A., Borrero, J. & Synolakis, C.E., 2004. The earthquake and tsunami of 1865 November 17: evidence for far-field tsunami hazard from Tonga, *Geophys. J. Int.,* **157**(1), 164–174.

Okal, E.A., Borrero, J.C. & Chagué-Goff, C., 2011. Tsunamigenic predecessors to the 2009 Samoa earthquake, *Earth-Sci. Rev.,* **107**(1-2), 128–140.

Okal, E.A., Reymond, D. & Hongsresawat, S., 2013. Large, pre-digital earthquakes of the Bonin-Mariana subduction zone, 1930–1974, *Tectonophysics,* **586,** 1–14.

Okal, E.A., Reymond, D. & Hébert, H., 2014. From earthquake size to far-field tsunami amplitude: development of a simple formula and application to DART buoy data, *Geophys. J. Int.,* **196**(1), 340–356.

PMEL, 2006. Method of Splitting Tsunami (MOST) software manual, Pacific Marine Environment Laboratory, National Oceanic & Atmospheric Administration.

Rabinovich, A.B., 1997. Spectral analysis of tsunami waves: separation of source and topography effects, *J. geophys. Res.,* **102**(C6), 12 663–12 676.

Reymond, D., Okal, E., Hébert, H. & Bourdet, M., 2012. Rapid forecast of tsunami wave heights from a database of pre-computed simulations, and application during the 2011 Tohoku tsunami in French Polynesia, *Geophys. Res. Lett.,* **39**(L11603), doi:10.1029/2012GL051640.

Salaree, A., 2019. Theoretical and computational contributions to the modeling of global tsunamis, *PhD Dissertation,* Northwestern University, 359 pp.

Salaree, A. & Okal, E.A., 2015. Field survey and modelling of the Caspian Sea tsunami of 1990 June 20, *Geophys. J. Int.,* **201**(2), 621–639.

Salaree, A. & Okal, E.A., 2018. The "tsunami earthquake" of 13 April 1923 in Northern Kamchatka: Seismological and hydrodynamic investigations, *Pure appl. Geophys.,* **175**(4), 1257–1285.

Satake, K., 1995. Linear and nonlinear computations of the 1992 Nicaragua earthquake tsunami, *Pure appl. Geophys.,* **144**(3–4), 455–470.

Satake, K., Shimazaki, K., Tsuji, Y. & Ueda, K., 1996. Time and size of a giant earthquake in Cascadia inferred from Japanese tsunami records of January 1700, *Nature,* **379**(6562), 246.

Satake, K., Wang, K. & Atwater, B.F., 2003. Fault slip and seismic moment of the 1700 Cascadia earthquake inferred from Japanese tsunami descriptions, *J. geophys. Res.,* **108**(2535), 17.

Scholz, C.H., 1982. Scaling laws for large earthquakes: Consequences for physical models, *Bull. seism. Soc. Am.,* **72**(1), 1–14.

Shuto, N., Suzuki, T. & Hasegawa, K., 1986. A study of numerical techniques on the tsunami propagation and run-up, *Sci. Tsunami Hazards,* **4,** 111–124.

Smith, S., 1999. *The Scientist & Engineer's Guide to Digital Signal Processing,* California Technical Pub.

Smith, W.H., 1993. On the accuracy of digital bathymetric data, *J. geophys. Res.,* **98**(B6), 9591–9603.

Smith, W.H. & Sandwell, D.T., 1994. Bathymetric prediction from dense satellite altimetry and sparse shipboard bathymetry, *J. geophys. Res.,* **99**(B11), 21 803–21 824.

Smith, W.H. & Sandwell, D.T., 1997. Global sea floor topography from satellite altimetry and ship depth soundings, *Science,* **277**(5334), 1956–1962.

Snedecor, G.W. & Cochran, W.G., 1937. *Statistical Methods,* Iowa State Press.

Stein, S. & Gordon, R.G., 1984. Statistical tests of additional plate boundaries from plate motion inversions, *Earth planet. Sci. Lett.,* **69**(2), 401–412.

Stein, S. & Okal, E.A., 2007. Ultralong period seismic study of the December 2004 Indian Ocean earthquake and implications for regional tectonics and the subduction process, *Bull. seism. Soc. Am.,* **97**(1A), S279–S295.

Stein, S., Spencer, B.D. & Brooks, E.M., 2015. Metrics for assessing earthquake-hazard map performance, *Bull. seism. Soc. Am.,* **105**(4), 2160–2173.

Stumpf, R.P., Holderied, K. & Sinclair, M., 2003. Determination of water depth with high-resolution satellite imagery over variable bottom types, *Limnol. Oceanogr.,* **48**(1, part 2), 547–556.

Synolakis, C.E., 1991. Green's law and the evolution of solitary waves, *Phys. Fluids A: Fluid Dyn.,* **3**(3), 490–491.

Synolakis, C.E., 2003. Tsunami and seiche, in *Earthquake Engineering Handbook,* pp. 9–1-9-90, eds Chen, W.-F & Scawthorn, C., CRC Press.

Synolakis, C.E. & Okal, E.A., 2005. 1992–2002: Perspective on a decade of post-tsunami surveys, tsunamis: case studies and recent developments, *Adv. Natur. Technol. Hazards,* **23,** 1–23.

Synolakis, C.E., Bernard, E.N., Titov, V.V., Kânoğlu, U. & González, F.I., 2008. Validation and verification of tsunami numerical models, *Pure appl. Geophys.,* **165,** 2197–2228.

Titov, V.V. & Synolakis, C.E., 1995. Modeling of breaking and nonbreaking long-wave evolution and runup using VTCS-2, *J. Waterway, Port, Coastal, Ocean Eng.,* **121**(6), 308–316.

Titov, V.V. & Synolakis, C.E., 1997. Extreme inundation flows during the Hokkaido-Nansei-Oki tsunami, *Geophys. Res. Lett.,* **24**(11), 1315–1318.

Titov, V.V., Kânoğlu, U. & Synolakis, C., 2016. Development of MOST for real-time tsunami forecasting, *J. Waterway, Port, Coastal Oceanic Eng.,* **142,** 03116004–1-03116004-16.

Tozer, B., Sandwell, D., Smith, W., Olson, C., Beale, J. & Wessel, P., 2019. Global bathymetry and topography at 15 arc sec: SRTM15+, *Earth Space Sci.,* **6**(10), 1847–1864.

Uyeda, S. & Kanamori, H., 1979. Back-arc opening and the mode of subduction, *J. geophys. Res.,* **84**(B3), 1049–1061.

Wessel, P. & Smith, W.H., 1991. Free software helps map and display data, *EOS, Trans. Am. Geophys. Un.,* **72**(41), 441 and 445–446.

Wronna, M., Baptista, M.A. & Miranda, J.M., 2019. Reanalysis of the 1761 transatlantic tsunami, *Nat. Hazards Earth Syst. Sci.,* **19**(2), 337–352.